Article

Union by Co-Lamination of Aluminum and Magnetic alloy obtained by Rapid Solidification

Francisco Garcia Almassio[1] , **Marcelo R. Pagnola**[1,2,]* , **Fabiana Saporiti**[1], and **Fernando Audebert**[1]

[1]   Facultad de Ingeniería de la Universidad de Buenos Aires, CABA, Argentina
[2]   CONICET - Universidad de Buenos Aires. Instituto de Tecnologías y Ciencias de la Ingeniería "Hilario Fernández Long" (INTECIN). Buenos Aires, Argentina.
*   Correspondence: mpagnola@fi.uba.ar

Abstract: The aim of this work is to study if it is possible to produce a joint by lamination of an Al-1050 plate and soft magnetic alloy ribbons, $Fe_{78}Si_9B_{13}(\%at.)$, obtained by a rapid solidification process by meaning the Melt Spinning (MS) technique. The material is characterized by X-Ray Diffraction, Optical, and Scanning Electron Microscopy, showing a mostly amorphous structure before and after the collamination. The typical defects caused by this rapid solidification technique are observed too, as well as the joint between materials. The magnetic characterization shows that the hysteresis curve of the ribbons has a H_c and a MS around 3.8 A/m and 1.44 T respectively. Therefore, by carrying out the compositional and chemical control together with the magnetic parameters, we can establish that it is possible to weld by lamination the magnetic alloy ribbons $Fe_{78}Si_9B_{13}(\%at.)$ with Al-1050 plates without the need for any filler materials.

1. Introduction

Ferromagnetic materials are a fundamental part of numerous equipment and devices of modern technology. Examples of these abound both in classical electrical machines and in the field of electronics. These can be divided into two groups based on the hysteresis behavior exhibited by these materials. Soft magnetic materials have high permeability at initial, low coercivity with high saturation in a hysteresis loop. These materials can be magnetized and demagnetized at low fields and with low hysteresis energy loss. Because of this, these materials can be used in power transmission, AC appliances, and magnetic shielding. Some applications of these are in different areas transformers, generators, motors, rotors, stators, filters, electromagnets, inductance cores, sensors, separators, brakes, and modules for telecommunications, and medical technology. On the other hand, the second group possesses high coercivity (H_c) with an M nearly

---

the same as saturation Melt Spinning (MS) in a hysteresis loop, these make it permanent 'magnets'. The magnetic energy that these materials can store is very high as possible. They are widely used in electric cars and telecommunications as well as sensors, biomedical detectors, transducers, storage disks, and advanced batteries.

More recently, the latter has become essential as components of the mechanisms used in clean technologies, particularly wind turbines and hybrid cars, as these can hold up to 200 magnets [1].

Since the last decades of the last century, a remarkable development in ferromagnetic alloys has been achieved with new compositions and production methods that open unprecedented technological, economic and ecological perspectives due to high yields. The possibility of weight and size reduction with a low impact on the environment of the equipment that contains them was due to the development of amorphous and nanocrystalline systems [2, 3]. Since these have improved the magnetic characteristics compared to crystalline systems [4, 5, 6]. Today, the urgent need to reduce environmental pollution worldwide has changed the situation, and just as at the time the oriented grain systems displaced products such as double pickled sheets due to their better efficiency, currently, amorphous and nanocrystalline materials are taking parts of the **FeSi** market due to the global pressure toward renewable energies. Most of these mentioned products are characterized by being used with alternating currents, so they lose energy through two independent mechanisms: hysteresis, due to the cyclical reorientation of the magnetic domains, and Foucault current, also known as eddy current. These losses can represent between 5% and 10% of the energy produced. This energy will manifest itself in the form of heat in the material, which must be correctly evacuated in order to ensure the proper functioning of the magnetic circuit in question. This is why in the industry a large number of magnetic circuits require welding and backing of Aluminum, due to its high thermal conductivity (k = 238 w/Km), low production cost, and weight ($\delta = 2.7$ g/cm^3) [7]. Due to the above, it is more common to find heat sinks composed entirely or largely of Aluminum in magnetic circuits. Thus, the present work is focused on lamination welds without the need for other materials, to increase the productivity in aluminum plates with magnetic parts. Taking as magnetic study material ribbons of $Fe_{78}Si_9B_{13}$(%at.) alloy was produced by rapid solidification by means of melt spinning (MS), which will allow us to obtain ribbons with an amorphous structure. These materials are very useful because they increase the magnetic induction by several orders of magnitude despite the process of obtaining from non-commercial scraps alloys with which the ribbons are made [3, 8].

The application of soft magnetic materials for the construction of high-efficiency electromagnetic cores has been limited until a few years ago for various reasons. One has been higher costs due to the value of some of the components of these systems and the need to introduce new manufacturing technologies in a market that was reasonably covered by traditional materials. Another is the almost zero demand for more ecological products. Today, these production costs have leveled off. Hence the importance of this work.

2. Experimental Procedure

2.1. Obtaining ribbons

The amorphous ribbons used in this work were obtained by the Melt Spinning process [8, 9, 10]. Figure 1 shows a schematic diagram and parameters of the melt-spinning process. The change of color corresponds to the solidification of the ribbon. Table 1 shows the parameters process with which these ribbons were produced:

Finally, the width (w) and thickness (t) of the ribbons were measured using a vernier caliper (Sensitivity: 0.02 mm.) and a micrometer (Sensitivity: 0.01 mm.), respectively. Ten (10) measurements were made at different points corresponding to 3 ribbons, obtaining the following values as an arithmetical average of those measurements; $w = 0.56 \pm 0.02$ mm and $t = 0.029 \pm 0.01$ mm.
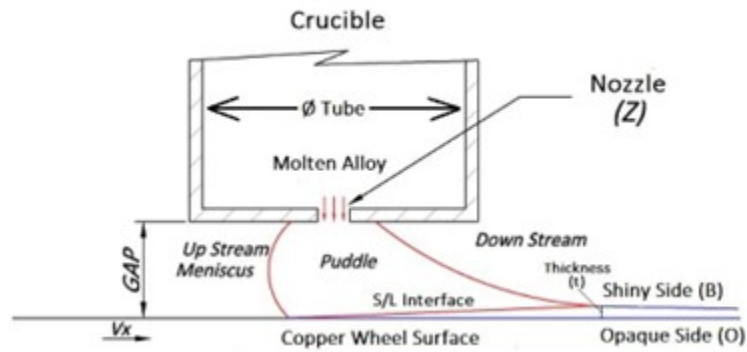
Figure 1. Melt Spinning Process and its parameters.

Parameter	Value
⌀Tube [mm]	16
⌀Nozzle [mm]	0.6
Ejection Pressure (P_{ey}) [bar]	0.3
GAP [mm]	4
Speed of Copper Wheel (v_x) [m/s]	30

Table 1. Values of the parameters used in the Melt Spinning process.

2.2. Collaminated samples

$Fe_{78}Si_9B_{13}$(%at.) ribbons were bonded by co-rolling with Al 1050 substrate to produce the collamination samples. To obtain these samples, four slabs of Aluminum 1050 (250X90 mm) were cut using a manual saw. An awl was then used to punch two slots in the center of about 20 mm in length. In addition to this, two of the substrate were sanded in the area where the amorphous alloy ribbons would rest and another two were left unsanded. Finally, the amorphous ribbons covering 10 mm of the width of the aluminum substrate (about 18 ribbons) were placed. These were punched through the slits and glued to the back of the aluminum plates with heat-resistant silicone sealant (Brand: Parsecs,resistant up to 300° C.). Two of the samples have the wheel size in contact with the substrate and the other two have the gas size in contact with the substrate. Figure 2 shows a front, side, and back view of the modeling of the specimens made in the *SolidWorks* program with their respective dimensions.

From the process mentioned in the first paragraph of this section, the following four samples were obtained:

- LB: The aluminum plate was not sanded and the ribbons were placed with the shiny side up.
- LO: The aluminum plate was not sanded and the ribbons were placed with the opaque side up.
- LBS: The aluminum plate was sanded and the ribbons were placed with the shiny side up.
- LOS: The aluminum plate was sanded and the ribbons were placed with the opaque side up.

Before co-lamination, the ribbons and the Aluminum 1050 substrate, were preheated for 30 min at a constant temperature of 200°C in an electric oven (Brand: O.R.L., model VIII.) to improve the resistance of the welding.

The four samples were passed through a twin-roller machine to obtain a thickness reduction of 30%. This is to ensure that the minimum threshold deformation is exceeded and thus achieve the correct welding between the ribbons and the aluminum. Likewise, the initial (e_o) and final (e_f) thicknesses were
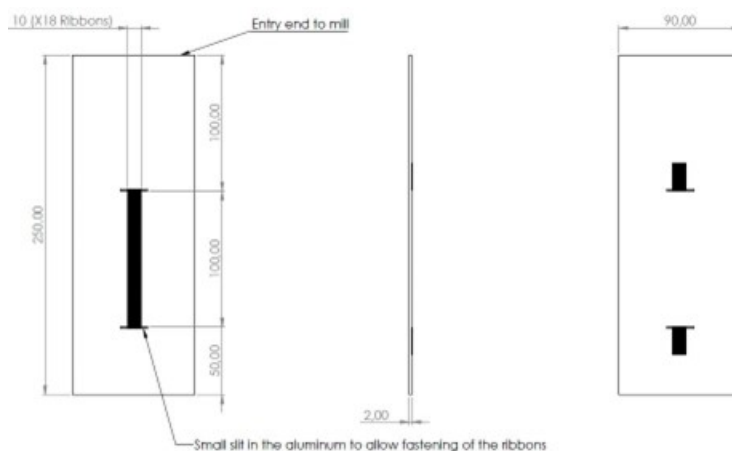
Figure 2. Front, side and back view of specimens to be collaminated.

measured using a vernier caliper (Sensitivity: 0.02 mm.) to calculate the reduction percent (The engineering deformation equation was used $\epsilon = \frac{e_f - e_o}{o}$) in each case, these values are shown in Table 2.

Samples	e_o [mm]	e_f [mm]	ϵ [%]
LB	2.10	1.40	33.3
LO	2.00	1.42	29.0
LBS	2.06	1.40	32.0
LOS	2.00	1.42	29.0

Table 2. Samples, initial e_o and final e_f thickness and reduction percentage for the 4 samples.

Structural characterization were carried out by means of X-ray diffraction (XRD), in a $\Theta - 2\Theta$ goniometer Rigaku equipped with a monochromator and a 1D detector, using Cu-K radiation (1.54056 $\dot{A}$). X-ray diffractograms were recorded in the 2Θ range of $10° - 100°$ with a step size of $0.05°$ at a scan rate of $0.5°$ /min. The metallographic examination was carried out by means of a ZEIZZ model EVO 10 scanning electron microscope (SEM) equipped with an Oxford Instrument energy dispersive X-ray (EDX) Ultim Max 40 model Silicon Drift Detector (SDD).

The thermal stability of the samples was analyzed by differential scanning calorimetry (DSC) on $Fe_{78}Si_9B_{13}$(%at.) as-cast ribbons was carried out with a Perkin Elmert, Pyris1DSC model equipment. The sample was weighed (5.0 mg) and then placed in an Al test crucible for comparison with a reference. Later, was heated from 25 to $630°C$ at a heating rate of $40°C$/min under an argon atmosphere.

Vickers microhardness test was carried out with durometer EMCO Test model Durascan 10 on as-cast ribbons and collaminated samples, 50 grams and 100 grams of load were applied for the ribbons and collaminated samples respectively and 15 s of dwell time.

A Magnetic hysteresis loop for the ribbon and collaminated samples was measured using a device that determines the magnetic properties by the induction method using a pair of coils (inductor and induced (pick-up), respectively) with a maximum applied field (H_{max}) of 500 A/m (for the ribbons) and 6000 A/m (for the collaminated samples). All cycles were obtained at a frequency of 50 Hz by applying either a sinusoidal magnetic field. In the case of magnetic losses, a sinusoidal magnetic flux is used by the determining.

3. Results

3.1. Microestructure characterization

The ribbons have a shiny side (B, a gas side) and an opaque side (O, wheel side) due to the difference in surface defects that exist between the surfaces in contact with the copper wheel, and the one that cools in the air (see Figure 1). Figure 3 shows X-ray diffractograms from the wheel side, gas side of the melt-spun ribbons and the heat treatment ribbons (TT).
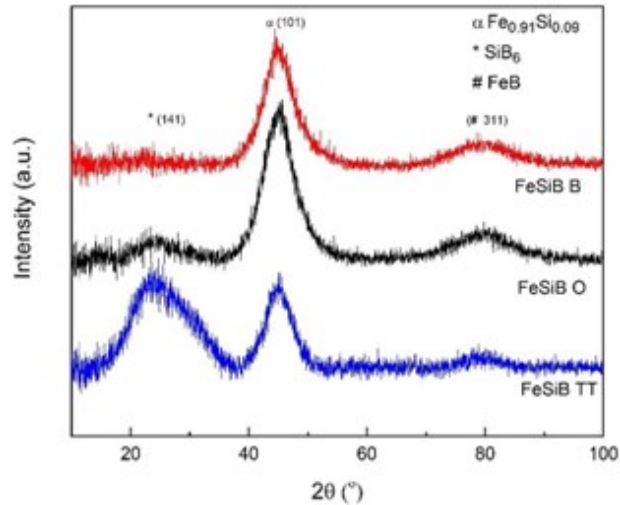
Figure 3. XRD diffractogram of both sides of the as quench ribbon (B, gas side; O, wheel side) and the heat treatment ribbon.

It can be seen that the as-quenched ribbon has a majority amorphous structure [11], for the **FeSi**-rich peak (1 0 1) with a nanocrystalline grain size of 1.6 ± 0.4 nm. In TT ribbon, can we observed a decrease in main a second peak an increase of the pre-peak comparing with the as-quenched ribbons, the size of the **FeSi**-rich nanocrystalline phase in the TT ribbons increase in order of 2 nm. The increase in (1 4 1) peak may be correspond to the segregation of a nanocrystalline phase (SiB_6). Minterwhile, the (1 0 1) and (3 1 1) peaks decreases your relative height, clearly induced by the heat treatment carried out on the ribbons. Table 3 indicates the diffractometry identification cards corresponding.

Elements	Peak	PDF Number	Reference
SiB_6	(1 4 1)	# 35-0809	[12]
$Fe_{0.91} \, Si_{0.09}$	(1 0 1)	#96-900-6909	[13]
FEB	(3 1 1)	# 32-0463	[14]

Table 3. Diffractometry identification cards.

Figure 4 shows optical image of the ribbons, where it can be seen that the width of the ribbons is about 0.6 mm.

Figure 5 shows secondary electron images of both surfaces of the melt-spun ribbons. The two surfaces of the ribbons, wheel side O and gas side B have well-differentiated characteristics.

Figure 5(a) and 5(b) show the rough surface of the wheel side, this is due to a large number of trapped gas bubbles between the liquid pool and the copper wheel, some imperfection of the wheel cylinder and dust particles can be observed. While the gas side presents a flat surface with slight undulations, dust particles
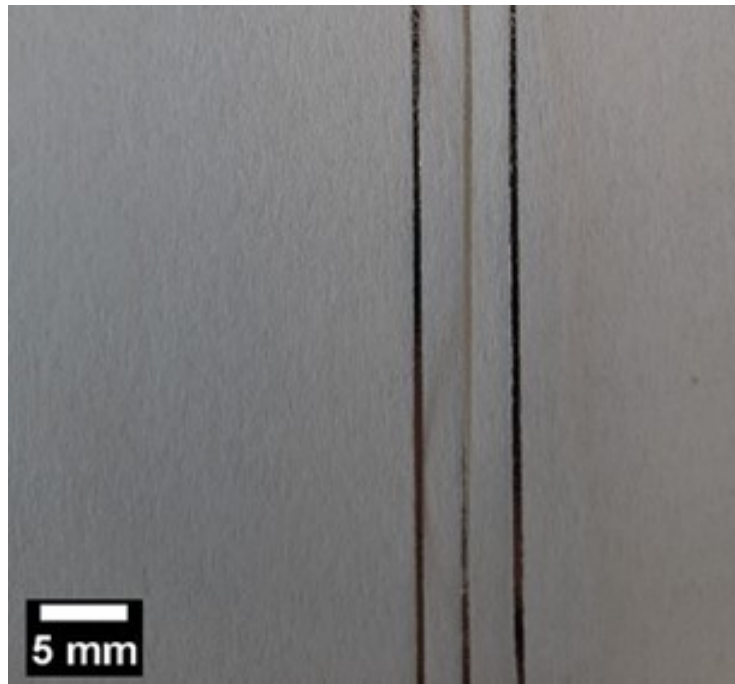
Figure 4. Optical image of $Fe_{78}Si_9B_{13}$(%at.) ribbons.

and oxides from the reaction between the alloy in the liquid state and the oxygen in the atmosphere due to the fact that the processing by melt spinning of the material was not carried out under inert atmosphere conditions (Helium, Argon, Nitrogen) or under vacuum, see Figure 5(c) and Figure 5(d).
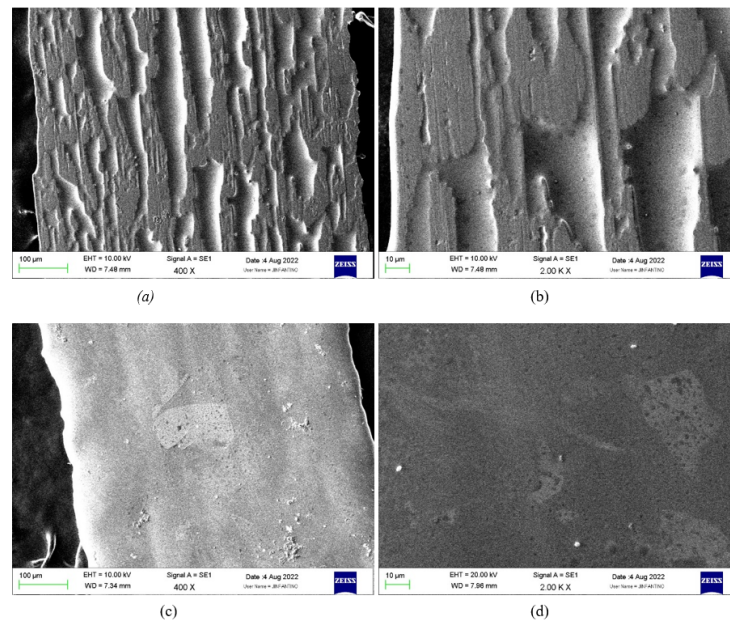
Figure 5. Second electron images of as-cast ribbon $Fe_{78}Si_9B_{13}$(%at.): (a) Side O, 400X and (b) Side O, 2000X wheel side and (c) Side B, 400X and (d) Side B, 2000X gas side.

Figure 6 shows optical images of the four collaminated samples. In all cases, after the lamination, the ribbons were bonded to the 1050 Aluminum substrate. However, only the LB and LO samples have a good

amount of ribbons remaining stuck from slot to slot. In the case of LBS and LOS many ribbons broke upon contact with the rolling mill and were scattered below the bottom slot or above the top slot.
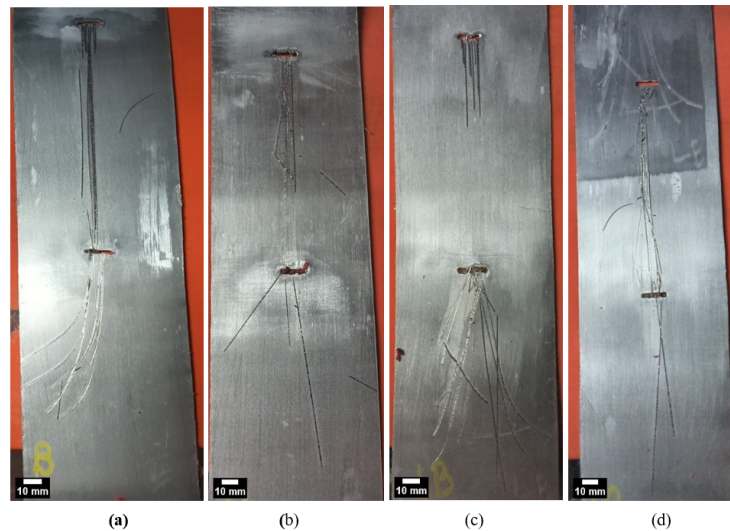
Figure 6. (a) LB, (b) LO, (c) LBS, (d) LOS. Optical images of the four-collaminated samples.

Figure 7 shows the ribbons surface of the collaminated samples. In all collaminated samples, the ribbons were cracked into small pieces in the normal direction of lamination.

Figure 7. Optical image of the samples after collamination.

In Figure 8(a) and 8(b) shows the surface of the amorphous ribbons $Fe_{78}Si_9B_{13}$(%at.) obtained by secondary electrons after the colamination process. All the samples show cracks, in most cases, these are normal to the collamination direction - Figure 8(a) and 8(b). In the upper part of the micrograph Figure 8(a) you can see the footprint left by a fragment of the ribbon on the aluminum substrate, it is believed that it came off during the cutting of the specimen using the manual saw.
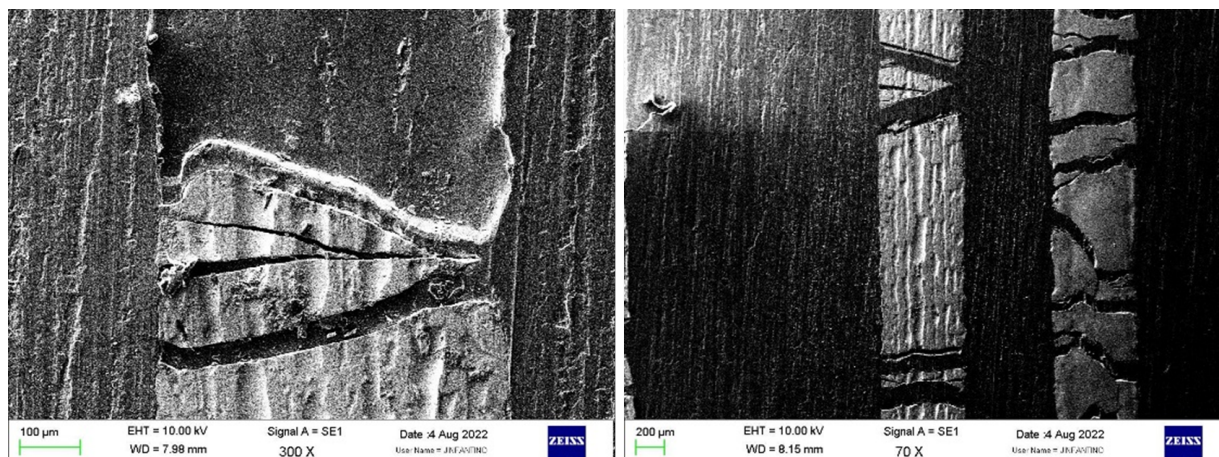
Figure 8. Second electron image of the surface of alloy $Fe_{78}Si_9B_{13}$(%at.) after colamination.

Figure 9 shows the micrographs of the cross-sections of the collaminated ribbons, to see the interface between the substrate and the ribbon obtained by secondary and backscattered electrons. The bright areas in the backscattered electrons images correspond to the ribbons as they have an atomic number, Z, higher than the average substrate (grey areas). In the different micrographs taken of the samples, especially at higher magnification , the absence of bond between the ribbons and the Al substrate can be observed, see Figure 9(a), 9(b) and 9(g). This lack of bond could cause the detachment of the ribbons when the sample was cut for its preparation due to some type of stress or vibration. In the backscattered electron micrographs taken of samples, especially at higher magnification, a certain amount of magnetic ribbon material (bright areas) can be observed not only in contact, but also was extruded inside the aluminum substrate in some zone not throughout the length of the joint. In Figures 9(e) and 9(h), it can be seen that the fracture of the tapes occurred throughout their thickness.

In Figure 10 we can see backscattered image in Figure 10(a), and 10(b) EDS (in spectrum 10 region) performed in the wheel side of a $Fe_{78}Si_9B_{13}$(%at.) as-cast ribbon. Elements such as **Fe**, **Si**, B, **F** and **Cr** can be appreciate in this sample.

- The composition of the ribbons is near of the theoretical. In some areas of the ribbons were measure **Cr** an **F** (spectrum 9 and 11 regions - see Figure 10(a)), this probably come from the blast furnace slag process corresponding to the type of raw material used [8]. The Boron concentration (%at) is lower than the theoretical.
- Table 4 shows the results of EDS analysis in atomic percent of wheel size of the as-cast ribbons.

Element	Atomic % Ribbons
B	11.09
Si	9.11
Cr	0.10
Fe	79.7

Table 4. EDS compositional analysis of as-cast ribbons (in spectrum 10 region).
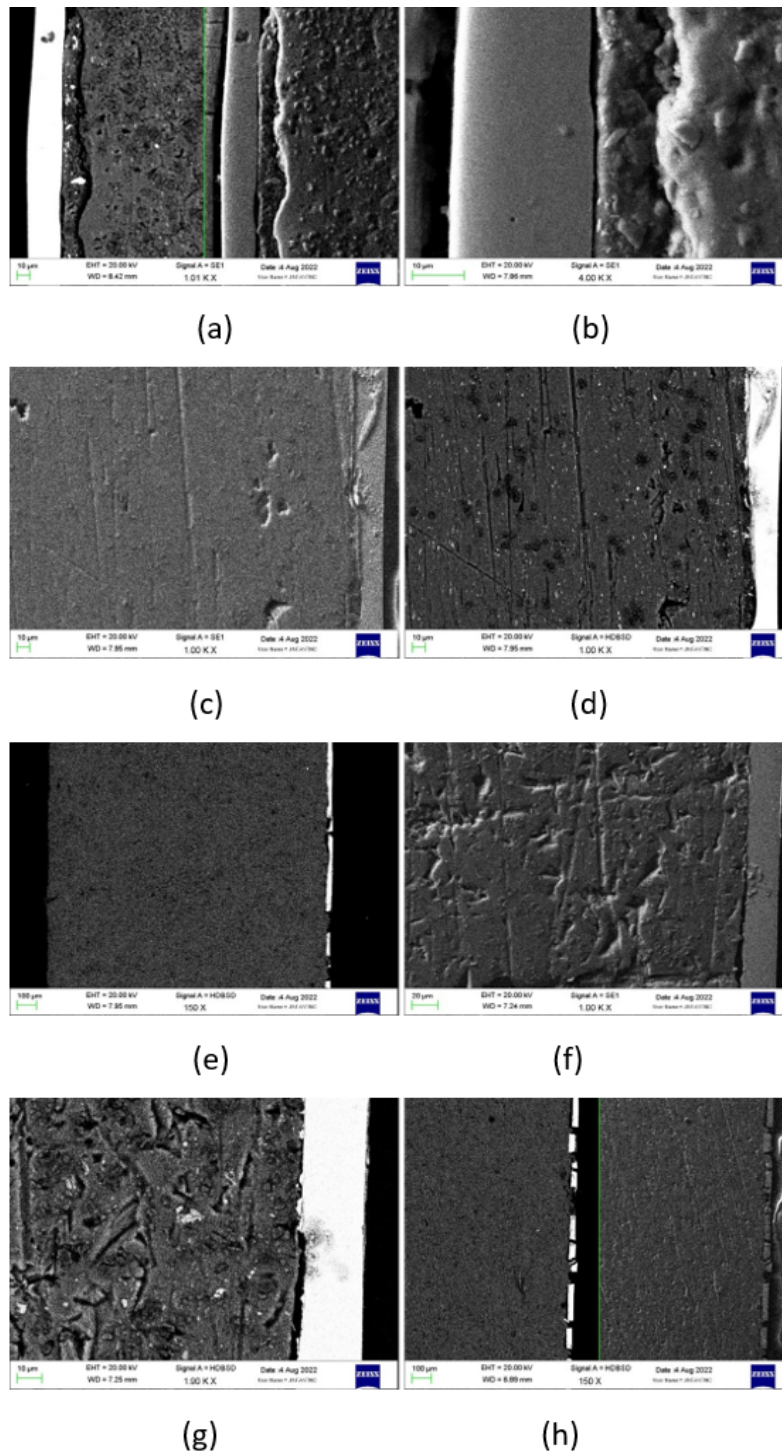
Figure 9. (a)Sample LB, (Left BSE; Right SE),(b) Sample LB, (SE),(c) Sample LBS, (SE),(d) Sample LBS, (BSE),(e) Sample LBS, (BSE),(f) Sample LOS, (SE),(g) Sample LOS, (BSE), (h) Sample LOS, (Left (BSE); Right (SE)).Images obtained by scanning electron microscopy SEM.(Backscattered Electron (BSE);Secondary Electron (SE).)
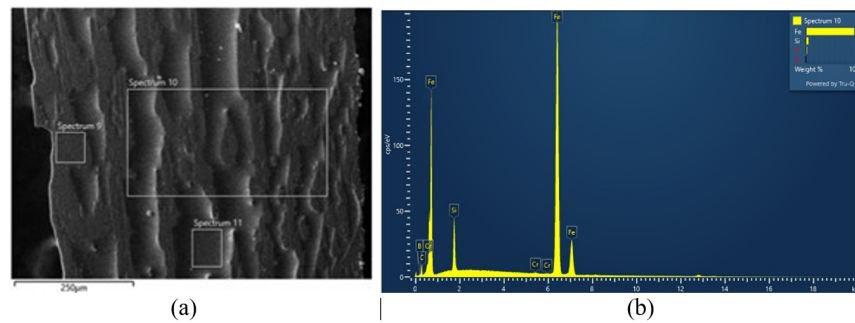
Figure 10. (a) Backscattered image of the as-cast ribbons,(b) EDS of the wheel size of the as-cast ribbons.Region and results of EDS analysis (spectrum 10).
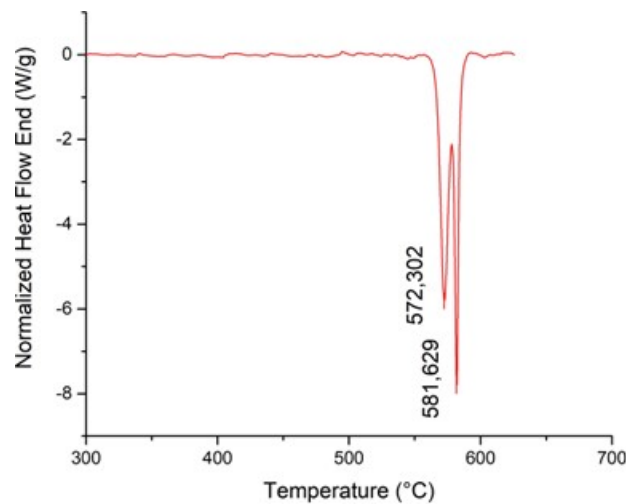
Figure 11. DSC curve of the as-cast ribbons $Fe_{78}Si_9B_{13}$(%at.).

3.2. Thermal analysis DSC

Figure 11, shows the DSC curves of the as-cast ribbons $Fe_{78}Si_9B_{13}$(%at.). Two exothermic peaks of irreversible reactions are observed. The first peak is near $572°C$, due to the amorphous **Si**-rich region that precipitates in a nanocrystalline composite $Fe_{0.91}Si_{0.09}$. Moreover, the second peak, near $582°C$, that be attributed to the increased number of B_β and $FeSi_2$ nanocrystals [8].

3.3. Vickers Microhardness testing

Table 5 shows the hardness of the as-cast ribbon (B,O) and the different collamination samples (LB, LBS, LOS). Comparing the results, it can be seen that there is an increase of 9% for the shiny side and 7% for the opaque side. In addition, it can be seen that the sanding of the aluminum substrate does not have to modify the hardness of the ribbons, but increase only the bond strength between the ribbon and the substrate

Figure 12 shows an indentation performed on a collaminated sample LB with the measures of both diagonals from which Vickers microhardness was calculated.

3.4. Magnetic Hysteresis Loop testing

The Magnetic Hysteresis Loop and Magnetic Losses for the as-cast ribbons are shown in Figure 13. We can see three different curves:

Sample	Hardness
B	1119 ± 62
O	1154 ± 55
LB	1220 ± 70
LBS	1233 ± 26
LOS	1238 ± 67

Table 5. Comparison of Vickers microhardness values obtained.
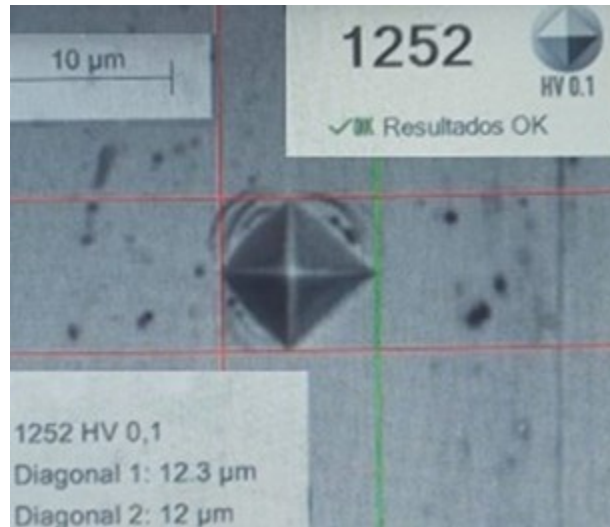
Figure 12. Indentation perform on sample LB.

- **Black Curve**: Cycle obtained by applying a sinusoidal magnetic field (H) at a frequency of 50 Hz.
- **Red Curve**: Cycle obtained by applying a magnetic field (H) in such a way that the magnetic response in the material (B and M) is sinusoidal. As states IEC (*International Electrotechnical Comission*) 404 "Standard for magnetic measurements methods in soft magnetic materials cores".
- **Blue Curve** (insert): Magnetic losses at 50 Hz as a function of the variation of the peak of M_{max} obtained as a response of the material. For this test, the density value of the tested material is necessary, using in this case 7.3 g/cm^3 [9].

We can observe that the values to take into account for this test are M_{max} = 1.44 T and H_c = 3.8 A/m. (The maximum term is used instead of saturation since if the curve is observed carefully; the material lacks a little to saturate). For the respective calculations, the section of the ribbon is 0.01624 mm^2. The results of Hc (Red curve) obtained are independent of the frequency of the applied field, minimizing the negative effects of the frequency since it simulates the application of a quasi-static field. On the other hand, for Figure 14 shows the hysteresis loop of collaminated samples and the as-cast (or as-cast) ribbon it can be observed the following curves:

Carrying out an analysis of magnetic hysteresis cycle areas can be observed that after the collamination process, there is an increase in the energy loss in the collaminated samples. This produces an evident degradation of the magnetic properties with an increase of six times in the coercive field. Meanwhile, something similar happens with the magnetization but decreases almost 16 times the value after collamination. In addition, it can be seen that the direction of easy magnetization abruptly changes, causing the curve not to achieve magnetic saturation.
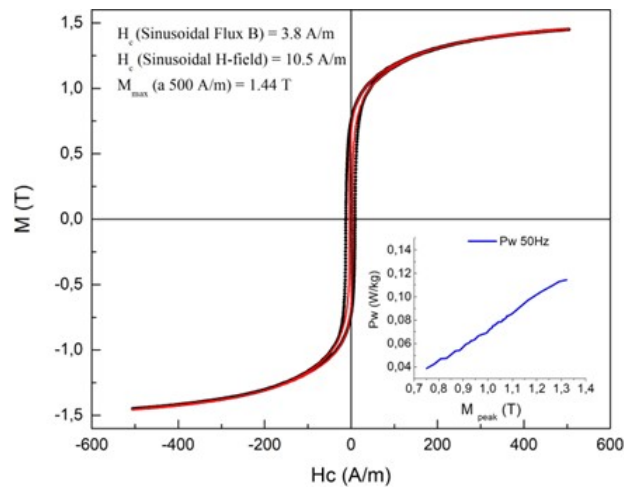
Figure 13. Magnetic Hysteresis Loop results for ribbons as-quenched.
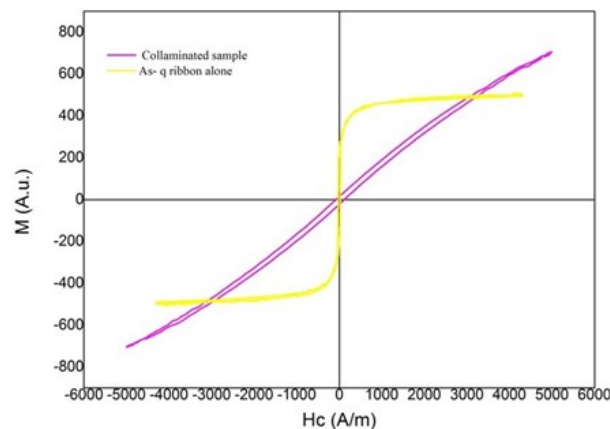
Figure 14. Magnetic Hysteresis Loop results for ribbons as-quenched and collaminated samples.

4. Discussion

- The diffractogram of as-cast ribbons (Figure 3) was compared with results obtained in [11] and [15]. Despite the differences in chemical composition and production parameters, in all three cases, the diffractograms resembles, showing a mostly amorphous material.

- The diffractograms of thermally treated (30 min at 200°C) ribbons show a much more marked pre-peak (corresponding to SiB_6 phase) in comparison to what was observed for the samples without the thermal treatment (Figure 3 curves black and red). This new short-range order could be related to a certain structural relaxation that the material underwent during the treatment, reaching more stable configurations due to the atomic motions caused by the temperature increase. This structural relaxation is accompanied by the change of many physical properties in the amorphous alloy, both mechanical and magnetic [16]. This phenomenon can also be related to annealing embrittlement [16, 17]. This embrittlement would be the main cause of the ribbons cracking during collamination.

- The Boron concentration (%at) observed by EDS (see Table 4) is less than the theoretical possibly because this element has a high melting point, and therefore its concentration after the melt spinning process is variable in the analyzed areas by this technique. Since the temperature values obtained to form the starting alloy are not reached again in the process of ribbons forming.
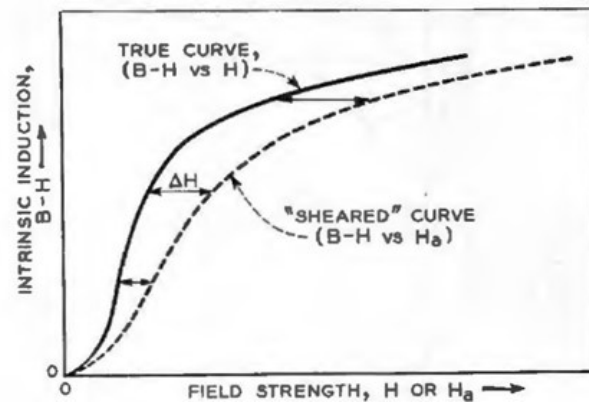
Figure 15. Effect of demagnetizing field on magnetic ribbon hysteresis loop [20].

- While the ribbons underwent a thermal treatment prior to collamination inducing a possible increase in hardness [11], the plastic deformation during this union also be considered since the amorphous alloys have been considered an ideal elastoplastic material. From this, we can infer that loss of free volume is another possible cause of hardening that takes place after stress relief. Therefore, this increase in hardness could be understood as a compression of the volume or elimination of defects in the material.

- The increased in short-range order (see X-ray diffractogram of section 3.1) may produce an increase of the hardness (see section 3.3) and the embrittlement in the sample after collamination and heat treatment.

- In Figure 11 of section 3.2 is not observable a first exothermic event ($T_{G,am}$ - Glass transition temperature) as expected in those alloys that contain only one metallic element. For this reason, it is not observed a well-defined T_c.

- Comparing the M_{max} and H_c obtained values in the as-cast ribbons received can be seen that the ours values are near to the obtained by other authors (see Table 6):

Source	M_s [T]	H_c [A/m]
paper	1.44	3.8
[18]	1.56	2.4
[19]	1.56	3.5

Table 6. Comparison of magnetic parameter.

In our case, the hysteresis loop does not reach saturation, which is why the value of M_s is low (See Figure 14). The decrease in the obtained value in the present work may also be due to the quality of the elements used to produce the master alloy [8].

- In the collaminated sample (see Figure 14), a large geometric anisotropy magnetic is present, due to the amorphous ribbons are cracked into small pieces causing the extension of continuous magnetic material to be a few millimeters (see Figure 7). This creates a demagnetizing effect on the sample due to the existence of free magnetic poles at the end of these small pieces. This field created is in the opposite direction of the applied field (H_a) (demagnetizing fields). The true field acting on a given section of the bar is the applied and demagnetizing field.

When B-H is plotted against H_a, the curve is lower than the B-H vs H curve (See Figure 15) and is said to be "sheared". The horizontal distance between them is proportional to B-H, as indicated. Taking this into account, which is what happens in Figure 14.

- The Biot numbers corresponding to the ejection process of magnetic ribbons are $Bi_{s/l} = 0.7$ and $Bi_A = 4.97x10^{-4}$ [21]. These obtained values are below the established limits $Bi_{s/l} > 1$ and $Bi_A > 7.2x10^{-4}$ [9] which prevented the typical case of cracking in the ribbons due to the convective phenomena generated during the melt-spinning process.

- The magnetic ribbon (white zone - see Figure 9d extruded inside the aluminum occurs in special point and not throughout the length of the joint. This confirms that the hardening of the surfaces, achieved by sanding the Aluminum in this case, facilitates the union between the phases in the collamination - Figure 9(c), 9(d), 9(e), 9(f), 9(g), 9(h).

- Free image analysis software called ImageJ(https://imagej.net/) was used to study the deformation of the ribbons after the co-lamination with the aluminum substrate from SEM images (see section 3.1). Concluding the following:

1. For the 3 samples the deformation, although it is significant, is less than the deformation of the collaminated assembly obtained (see Table 2), this makes sense if one takes into account that Aluminum is much more ductile than the ribbons because of having **Fe** as their main component.

2. The significant values of plastic deformation obtained reaffirm that amorphous alloys behave as an ideal elasto-plastic material, presenting very low strain hardening.

3. Another significant point is that when comparing the deformation obtained between the samples with the sanded aluminum plate (LBS and LOS , Figure 9(d) and 9(g)) and the unsanded samples (LB, Figure 9(b) there is an observable difference, with the former having a clearly higher value. Although no bibliography was found to explain this phenomenon, it can be inferred that brushing can generate a hardened layer (*scratch-brushed layers*), which breaks easily during collamination due to its fragility and this is what allows the flow of virgin material from the materials to join. This flow is synonymous with deformation and it occurs precisely in the direction of the thickness of the amorphous alloy ribbons. Hence, the surface preparation of the substrate to be coated influences the calculated deformation in the samples.

5. Conclusions

From the tests carried out in this work detailed in Section 3, it is possible to conclude that the objectives were met, according to:

1. The welding between the magnetic alloy ribbons $Fe_{78}Si_9B_{13}$(%at.), obtained from non-commercial scrap alloys, and Al-1050 plates without any filler materials, has been able to develop by lamination (See Figure 6(a), 6(b), 6(c) y 6(d)). The bond was corroborated by SEM images, which show extruded ribbon material within the aluminum substrate (See Figure 9d). Also, the deformation analysis performed by the ImageJ software show that when the collaminated samples were cut the ribbons remained welded

2. The samples maintained a mostly amorphous structure after the heat treatment required for the collamination (See Figure 3).

However, some undesired effects do occur, such as in the hysteresis loop, that shows an important amount of magnetic anisotropy in the collaminated samples in comparison with as-quenched ribbons (See Figure 14). Nevertheless, it is possible to improve the magnetic efficiency achieved by proposing a set of modifications in different parameters in order to avoid the cracking of the magnetic ribbons during the collamination:

1. Decreasing heat treatment temperature and time prior to co-lamination may avoid temper brittleness.
2. Modifying the copper wheel speed and a controlled atmosphere in melt-spun process (see Figure 1).
3. Decreasing the lamination reduction coefficient (ϵ) and the substrate thickness would reduce the tensile stresses in the amorphous ribbons during collamination.

Acknowledgments

Disclosure statement: The authors declare no conflict of interest. The funders had no role in the design of the study; in the collection, analyses, or interpretation of data; in the writing of the manuscript; or in the decision to publish the results.

References

[1] M. Pagnola and H. Sirkin. Materiales magnéticos modernos, May 2018. Avaliable at https://www.revistapetroquimica.com/materiales-magneticos-modernos/.

[2] D Muraca, J Silveyra, M Pagnola, and V Cremaschi. Nanocrystals magnetic contribution to finemet-type soft magnetic materials with ge addition. *Journal of Magnetism and magnetic Materials*, 321(21):3640–3645, 2009.

[3] Marcelo R Pagnola, Marcelo Barone, Mariano Malmoria, and Hugo Sirkin. Influence of z/w relation in chill block melt spinning (cbms) process and analysis of thickness in ribbons. *Multidiscipline Modeling in Materials and Structures*, 2015.

[4] KH J. Buschow. *J. Appl. Phys.*, 53:7713, 1982.

[5] Giselher Herzer. Modern soft magnets: Amorphous and nanocrystalline materials. *Acta Materialia*, 61(3):718–734, 2013.

[6] Pu Wang, Min Wei, Yannan Dong, Zhengqu Zhu, Jiaqi Liu, Jing Pang, Xiaoyu Li, and Jiaquan Zhang. Crystallization evolution behavior of amorphous fe85. 7si7. 9b3. 6cr2c0. 8 powder produced by a novel atomization process. *Journal of Non-Crystalline Solids*, 594:121824, 2022.

[7] R. A. Serway and J. W. Jewett. *Physics I, 3rd Edition*. Cengage Learning Ed, 2004.

[8] Marcelo R Pagnola, Mariano Malmoria, Marcelo Barone, and Hugo Sirkin. Analysis of fe78si9b13 (% at.) ribbons of noncommercial scrap materials produced by melt spinning equipment. *Multidiscipline Modeling in Materials and Structures*, 2014.

[9] M Pagnola, M Malmoria, and M Barone. Biot number behaviour in the chill block melt spinning (cbms) process. *Applied Thermal Engineering*, 103:807–811, 2016.

[10] Marcelo Rubén Pagnola, Jairo Useche Vivero, and Andres Guillermo Marrugo. *New uses of micro and nanomaterials*. IntechOpen, 2018. Avaliable at https://www.intechopen.com/books/6851.

[11] A Cabral-Prieto, F García-Santibáñez, A López, R López-Castañares, and O Olea Cardoso. Vickers microhardness and hyperfine magnetic field variations of heat treated amorphous fe78si9b13 alloy ribbons. *Hyperfine Interactions*, 161(1):69–81, 2005.

[12] NN Zhuravlev. X-ray determination of the structure of sib. *Kristallografiya*, 1(6):666–68, 1956.

[13] J Zhang and F Guyot. Thermal equation of state of iron and fe0. 91si0. 09. *Physics and Chemistry of Minerals*, 26(3):206–211, 1999.

[14] Sterling B Hendricks and Peter R Kosting. Xxxv. the crystal structure of fe2p, fe2n, fe3n and feb. *Zeitschrift für Kristallographie-Crystalline Materials*, 74(1-6):511–533, 1930.

[15] Narges Amini, Július Dekan, Milan Pavúk, Safdar Habibi, and Marcel Miglierini. Influence of quenching rate on the structure, morphology, and hyperfine parameters of amorphous ribbons. *Journal of Electrical Engineering*, 67(5):365, 2016.

[16] Aleksandr Markovich Glezer and NA Shurygina. *Amorphous-nanocrystalline alloys*. CRC Press, 2017.

[17] JM Cadogan, SJ Campbell, J Jing, CP Foley, P Kater, and YW Mai. Annealing embrittlement of fe78si9b13 (metglas-2605s2). *Hyperfine Interactions*, 226(1):7–14, 2014.

[18] Teruo Bitoh, Akihiro Makino, and Akihisa Inoue. Origin of low coercivity of fe-(al, ga)-(p, c, b, si, ge) bulk glassy alloys. *Materials transactions*, 44(10):2020–2024, 2003.

[19] A Makino, T Bitoh, A Kojima, A Inoue, and T Masumoto. Low core losses of nanocrystalline fe–zr–nb–b soft magnetic alloys with high magnetic flux density. *Materials Science and Engineering: A*, 304:1083–1086, 2001.

[20] Richard M Bozorth. *Ferromagnetism*. Wiley-IEEE Press, 1993.

[21] F. Garcia Almassio. *Unión por Co-Laminación de Aluminio y aleación Magnética obtenida por Solidificación Rápida*. Universidad de Buenos Aires, 2019.